

This is an Open Access document downloaded from ORCA, Cardiff University's institutional repository:<https://orca.cardiff.ac.uk/id/eprint/106098/>

This is the author's version of a work that was submitted to / accepted for publication.

Citation for final published version:

Khasu, Motlokoa, Nyathi, Thulani, Morgan, David , Hutchings, Graham , Claeys, Michael and Fischer, Nico 2017. Co₃O₄ morphology in the preferential oxidation of CO. *Catalysis Science & Technology* 7 (20) , pp. 4806-4817. 10.1039/C7CY01194F

Publishers page: <http://dx.doi.org/10.1039/C7CY01194F>

Please note:

Changes made as a result of publishing processes such as copy-editing, formatting and page numbers may not be reflected in this version. For the definitive version of this publication, please refer to the published source. You are advised to consult the publisher's version if you wish to cite this paper.

This version is being made available in accordance with publisher policies. See <http://orca.cf.ac.uk/policies.html> for usage policies. Copyright and moral rights for publications made available in ORCA are retained by the copyright holders.



Co₃O₄ morphology in the preferential oxidation of CO

Motlokoa Khasu, Thulani Nyathi, David J. Morgan, Graham J. Hutchings, Michael Claeys, Nico Fischer*

*Catalysis Institute and e*change (DST-NRF Centre of Excellence in Catalysis), Department of Chemical Engineering, University of Cape Town, Rondebosch 7701, Cape Town, South Africa, *nico.fischer@uct.ac.za*

ARTICLE INFO

ABSTRACT

Key words:

Preferential
oxidation of CO

In situ
characterization

Morphology

Magnetometer

XRD

The preferential oxidation (PrOx) of carbon monoxide is an effective process for the removal of trace amounts of CO in a hydrogen-rich gas stream originating from steam reforming or gasification processes. CO can act as catalyst poison in various downstream processes such as the ammonia synthesis or PEM fuel cells for power generation. The effect on activity and selectivity of different cobalt oxide morphologies (cubes, sheets and belts) in Co₃O₄/SiO₂ model catalysts was studied against conventional near-spherical nanoparticles. With a combination of offline and specialized in situ characterisation techniques the stability and catalytic performance of the model catalysts was monitored. With TEM and XRD, the prepared nanosheets and nanobelts were identified as superstructures constituted by small crystallites with similar catalytic activity to conventional nanoparticles. The nanocubes however, consisting of single crystals or at least large crystalline domains, display a superior surface specific CO oxidation activity which is attributed to the preferential exposure of {001} planes. Catalytic sites on these plains seem to support the formation of the Co^{3+/2+} redox pair required for the underlying Mars-van Krevelen mechanism.

1 Introduction

Due to their quick start-up at low operating temperatures, feasible reduction kinetics and physically strong solid electrolyte membrane, hydrogen fuelled proton exchange membrane fuel cells (PEMFCs) are of high interest as power generation devices in a multitude of applications [1]. One major challenge of PEMFCs is to avoid catalyst deactivation via small amounts (>10 ppm) of carbon monoxide in the hydrogen stream [2]. Hydrogen is usually produced via gasification or partial oxidation [1,3], steam reforming (STR) [4], dry reforming [4], or autothermal reforming (ATR) [3] of lighter oil fractions, coal, natural gas and biomass. The products of these processes are naturally H_2 , CO_2 and a noticeable amount of CO (2-5 vol.-%). The obtained gas stream is subsequently treated in a high temperature and a low temperature water-gas shift (WGS) reaction to reduce CO content to 0.5-1 vol.-%. Although lowered, these levels are still intolerable for a number of applications. CO can be further removed by the selective hydrogenation of CO to CH_4 [5] or the preferential oxidation of CO through catalytically converting CO to CO_2 with co-fed oxygen over noble and/or transition metals [6]. In the present study, we focus on the latter process, as in case of a selective catalyst, no desired reactant, i.e. H_2 , is consumed in the reaction.

Noble metals, although studied intensively and active in the reaction, have the intrinsic challenge of high costs and limited availability. The attention has therefore shifted to transition metal catalysts such as copper and cobalt oxide based catalysts as non-noble-metal alternatives [11,12]. Cu-based catalysts show high activity even at low temperatures, but are reported to suffer from a narrow temperature range of operation (50-160°C) as well as deactivation in the presence of CO_2 and H_2O . Catalyst instability and a resulting poor selectivity at higher temperatures remain to be overcome [13,14, 15]. In contrast, cobalt oxide based catalysts have a good prospect for the CO PrOx reaction in excess H_2 by offering a wide temperature window for operation, good selectivity. These properties are influenced by the good redox properties of Co_3O_4 which in part result from its spinel structure, with the active Co^{3+} in an octahedral position and the less active Co^{2+} in a tetrahedral coordination [16]. The resulting redox pair can support the Mars-van Krevelen mechanism proposed to govern the oxidation of CO over transition metal oxides [17]. Mechanistic

studies on CO oxidation in excess hydrogen indicate that Co_3O_4 is active for CO oxidation, but at elevated temperatures, the reduction of the spinel oxide to CoO and metallic Co^0 represents the dominating deactivation process [18]. It is of essential importance to understand the deactivation process of these catalysts and its effect on catalyst performance under CO-PrOx conditions. As reported by Nyathi et al. [22], it is expected that upon reduction to the zero valent metallic Co, the dominating catalytic mechanism shifts from a Mars van Krevelen based CO oxidation to a classic methanation in combination with hydrogen oxidation. Deactivation via reduction can potentially be prevented or suppressed by using cobalt oxide with strong-metal support interaction with a defect forming support such as SiO_2 [19, 20].

The ultimate performance of catalytic nanoparticles strongly depends on their size and morphology/shape [21]. The effect of size of Co_3O_4 nanoparticles has already been substantiated by Nyathi et al. [22] using differently sized Co_3O_4 crystallites with a narrow size distribution supported on $\gamma\text{-Al}_2\text{O}_3$ as model catalysts. Regarding morphology, it is important to understand the relationship between catalyst morphology and activity. A lot of work has been reported on the development of synthetic routes with controlled morphologies and dimensionality to expose well defined crystal planes which are commonly not exposed in conventional near-spherical nanoparticles [23–25]. Hu et al. [23] report on the preparation of Co_3O_4 nanobelts, nanosheets and nanocubes with preferentially exposed planes of $\{011\}$, $\{112\}$ and $\{001\}$ respectively by a hydrothermal method using cobalt hydroxide as a precursor. The nanobelts with a $\{112\}$ crystal plane show higher activity when compared to the $\{011\}$ and $\{001\}$ planes in the catalytic combustion of methane. There are reports on the effect of morphology in the CO oxidation reaction (in the absence of H_2) [21,24,41,42] describing an enhanced activity on $\{011\}$ planes vs $\{100\}$ planes, but to the best of our knowledge no study has investigated the morphology dependency in H_2 rich atmospheres and therefore taking a potential morphology dependent deactivation, i.e. reduction into account.

In this study, nanobelts, nanosheets and nanocubes were prepared via hydrothermal and precipitation based techniques, and tested for the CO oxidation in excess hydrogen. The dimensions of the different morphologies were chosen (50-300 nm) to minimize the possible effect of corner and edge atoms on activity

and selectivity. Conventional nanoparticles synthesised in our group [22] were used as a baseline to demonstrate that morphologically orientated crystallites can exhibit higher CO oxidation activity than near spherical nanoparticles.

2 Experimental

Co₃O₄ nanocubes and nanosheets were prepared via a hydrothermal technique, while the nanobelts and silica support were prepared via a precipitation based technique.

2.1 Catalyst preparation

2.1.1 Nanocubes

The method reported by Hu et al. [23] describes the preparation of cubic Co₃O₄ nanoparticles. 0.291 g of Co(NO₃)₂·6H₂O (Sigma Aldrich 98% purity) is dissolved in 20 ml of ethanol (Kimix) yielding a 0.001 M red solution. Subsequently a mixture of 2 ml octadecenylamine (ACROS Organics 90% purity) and 10 ml of ethanol (Kimix) is added dropwise and left stirring for 30 min. A colour change from red to green is observed as β-Co(OH)₂ is formed. The solution is subsequently transferred into eight 40 ml Parr acid digestion autoclaves (Parr Instrument Co) equipped with a Teflon liner, sealed and fixed in a rack. The rack is mounted on a rotating shaft in an oven (RKC Instrument Inc.) and heated to 180°C for 12 hours. After cooling, a black paste is obtained which is sequentially washed five times with ethanol and water. The sample is dried under vacuum (100 mbar) at 60°C overnight using a rotary evaporator (R-210/215 BUCHI) and calcined in a Nabertherm furnace at 350°C for 3 hrs to yield Co₃O₄ nanocubes.

2.1.2 Nanosheets

The synthesis technique reported by Hu et al. [23] and described in section 2.1.1 to synthesise Co₃O₄ cubes can be modified slightly to yield nanosheets. Co(NO₃)₂·6H₂O (Sigma Aldrich 98% purity) is dissolved in deionised water instead of ethanol. The subsequent steps remain identical.

2.1.3 Nanobelts

A direct and scalable synthesis of nanobelts is reported in the work of Wang et al. [25]. 0.1 g of $\text{Co}(\text{NO}_3)_2 \cdot 6\text{H}_2\text{O}$ (Sigma Aldrich, 98% purity) and 0.6 g of urea are mixed in 10 ml of deionized water. The solution is rapidly heated to 95°C in a watch glass covered beaker and maintained at the set temperature for 12 hours under stirring. A pink precipitate is collected after cooling, re-suspended in deionised water and centrifuged in a Sorvall RC 5C Plus Centrifuge (5000 rpm, 10 min) five times and subsequently dried at 50°C in a Memmert oven overnight. The resulting $\beta\text{-Co}(\text{OH})_2$ nanobelts are calcined at 250°C in static air to yield Co_3O_4 nanobelts.

2.1.4 Synthesis of Nanoparticles

The preparation technique is described in detail elsewhere [22, 26, 27]. In short, 250 g of n-hexane (AR grade, Kimix) are combined with 25 g of non-ionic surfactant penta-ethyleneglycol-dodecylether (Berol 050 Akzo Nobel) and stirred for 1 hour at 800 rpm (Caframo RZR-1 overhead stirrer). A solution of 3.3 g of $\text{Co}(\text{NO}_3)_2 \cdot 6\text{H}_2\text{O}$ (Sigma Aldrich, 98% purity) in 15 ml deionized water is added dropwise to the n-hexane-PEDGE mixture under stirring. A clear pink solution forms indicating the stability of the reverse micelles. 25 wt.% NH_3 aqueous solution ($\text{NH}_3:\text{Co}^{2+}$ ratio of 4:1) is added dropwise over a period of 30 minutes, upon which a colour change from red to light-green is observed indicating the formation of $\text{Co}(\text{OH})_x$. The reverse micelles are not destabilised by this treatment and essentially retain the precipitate in their confined geometry. The destabilization of the micelles and flocculation of the precipitate is achieved via the addition of acetone (Kimix). After settling, the precipitate is separated and washed several times with acetone. The washed solid is dried at room temperature in air and subsequently calcined at 200°C in a Nabertherm furnace yielding a black powder (Co_3O_4).

2.1.5 Support - Stöber SiO_2 spheres

A seeded growth technique to synthesise monodisperse SiO_2 spheres (diameter of $150\text{ nm} \pm 5\%$ to $1.2\text{ }\mu\text{m} \pm 1\%$) is reported by Stöber and Fink [28]. A solution of 0.5 ml TEOS (Sigma Aldrich reagent grade, 98%)

and 2 ml of ethanol (Kimix) is quickly mixed with 50 ml of ethanol and 10 ml of 25 wt.-% ammonia (Kimix) under stirring and left to age for two hours.

A third solution containing 7 ml of TEOS and 28 ml of ethanol is transferred dropwise into the mixture under stirring and left to age for another two hours. The resulting white precipitate is washed with ethanol five times and dried at 60°C in a rotary evaporator (100 mbar) overnight.

2.2 Supporting the catalyst

The prepared Co_3O_4 nanoparticles are loaded onto the synthesised SiO_2 support via a physical mixing procedure (target 5 wt.-% Co_3O_4 loading) [22, 26, 27]. Co_3O_4 nanoparticles are initially suspended in deionised water for 1 hour in an Erlenmeyer flask to reduce the degree of agglomeration. Under stirring, the support is added slowly to the suspension over 10 minutes. Prior to the addition of the support, the SiO_2 spheres were dried in a Nabertherm furnace at 350°C for 3 hours to reduce residual moisture. After an additional sonication treatment of 1 hour, the supernatant is dried off in a rotary evaporator (50 rpm, 60°C, 100 mbar) overnight.

2.3 Catalyst characterization

2.3.1 X-ray Diffraction

Crystalline phases were analysed using X-ray diffraction (XRD) on a Bruker AXS D8 Advance X-ray laboratory diffractometer operated at 35 kV and 40 mA equipped with a Co source ($\lambda_{\text{Co-K}\alpha 1} = 1.78897 \text{ \AA}$) and a VANTEC position-sensitive detector (Bruker AXS). Analysis were performed on both unsupported and supported samples with a scan range of 20° to 130° 2θ , a step-size of 0.01° and a scan rate of 0.025°/s. The diffraction peaks of the samples obtained were analysed against the peaks positions and intensities of reference patterns recorded in the ICDD PDF2 2006 database. The *in situ* studies were performed in a XRD cell developed at the University of Cape Town described in detail elsewhere [29, 30] with a scan range of

40° to 80° 2 θ , a step size of 0.03083045° and a scan rate of 0.025°/s. The employed reaction conditions are given in section 2.4.

2.3.2 *Transmission Electron Microscopy*

A Tecnai F20 transmission electron microscopy (TEM) equipped with a field emission gun (operated at 200 kV) was used to determine the size distribution and morphology of the prepared samples. The morphology, crystallite size and size distribution was obtained from the as prepared Co₃O₄. The distribution on the carrier as well as potential morphological changes after exposure to reaction conditions were studied on the supported samples. For the sample presentation, a small volume of solid is re-suspended in acetone using ultrasonication. A droplet of the supernatant is transferred onto a holey carbon coated copper grid and dried in air for about 10 minutes before analysis.

2.3.3 *Temperature Programmed Reduction*

The reduction behaviour of the model catalysts was studied by temperature programmed reduction (TPR) in a diluted hydrogen stream (Micromeritics AutoChem2910). About 100 mg of SiO₂ supported Co₃O₄ was loaded into a quartz reactor and dried in flowing argon (10 mL (NTP)/min) at 110°C (heating rate: 10°C/min) for 60 minutes. Subsequently the system was cooled to 60°C upon which a gas flow of 5% hydrogen in argon (50 mL (NTP)/min) was allowed to flow through the sample. The hydrogen consumption was monitored with a thermal conductivity detector (TCD) while ramping the temperature to 900°C (heating rate: 5°C/min).

2.3.4 *X-ray Photoelectron Spectroscopy*

X-ray Photoelectron Spectroscopy (XPS) measurements were performed on a Kratos Axis Ultra DLD photoelectron spectrometer utilising monochromatic Al radiation (1486.6 eV photon energy). All data was acquired at a pass energy of 40 eV for high resolution spectra and 160 eV for survey scans; the step size was 0.1 eV for high resolution scans whilst 1 eV was used for the survey scans. Charge compensation was

achieved using the Kratos immersion lens system and all spectra were subsequently calibrated to the C(1s) line taken to be 284.8 eV.

For gas treatments, the samples were pressed into discs and placed in a gold-plated cup before being inserted into a Kratos catalysis cell and subsequently evacuated to ca. 10^{-7} mbar. The samples were heated under gas flow (1 bar pressure) to the desired temperature and the reaction was quenched (if necessary) by swapping to a high purity argon gas feed to purge the system and cooling down under this stream.

Data analysis was performed using CasaXPS software (v2.3.17 PR1.1) utilising sensitivity factors from the manufacturer. Due to the complex nature of the Co(2p) peak envelope [39], peak shapes derived from standard materials (Co metal, CoO and Co₃O₄) were used for fitting the spectral envelopes.

2.3.5 Atomic Absorption Spectroscopy (AAS) and Inductively Coupled Plasma mass spectrometry (ICPMS)

To determine the metal loading of Co₃O₄ on silica, both atomic absorption spectroscopy (AAS) and inductively coupled plasma mass spectrometry (ICPMS) were applied. For AAS analysis, the model catalysts were digested in a mixture of acids (6 mL concentrated hydrochloric acid (HCl), 2 mL concentrated hydrofluoric acid (HF), 2 mL concentrated nitric acid (HNO₃)) in a MARS-5 Microwave digester. Analysis was then carried out on a Varian SpectrAA-110 series instrument.

For the ICPMS analysis, the sample is digested in 3 ml of HCl, 3 ml of HF and a few drops of HNO₃ in a reactor containing bi-distilled water. The mixture is subsequently heated to 130°C, stirred for an hour and then cooled under a jet of water. To avoid any residue, 60ml of H₃BO₃ is added under stirring. The solution is subsequently filtered and transferred to a volumetric flask. The solution is injected into a Varian OES 730 Series instrument.

2.3.6 Brunauer-Emmett-Teller

The specific surface areas of the support and the prepared Co_3O_4 samples were determined using the Brunauer-Emmett-Teller (BET) method based on physical adsorption and capillary condensation (Micromeritics TriStar 3000). The sample was cooled to liquid nitrogen temperature, followed by physical absorption (based on van der Waals interactions) of N_2 of a known amount of gas onto the surface of the sample. From the amount of adsorbed gas, assuming a monomolecular coverage, the surface area is calculated.

2.4 Catalyst testing conditions

The prepared different morphology Co_3O_4 nanoparticles as well as the 'conventional' nanoparticles were supported on SiO_2 with a targeted Co_3O_4 loading of 5 wt.-% (see section 2.2). The CO-PrOx reaction was carried out in a fixed bed reactor mounted in an in house developed magnetometer. Details on the working principles of the magnetometer can be found elsewhere [22, 30, 31, 32, 39]. It must be noted that under reaction conditions the only ferromagnetic material in the tested catalytic materials is metallic cobalt. Therefore, the magnetic signal can be directly and quantitatively be related to metallic cobalt in the sample. The feed and reactor outlet gases were analysed via an online Varian CP-4900 micro-GC. Experiments were performed at atmospheric pressure with a space velocity of 120000 ml/(g.hr) and CO: O_2 volumetric ratio of 1:1 using a pre-mixed gas (1% CO, 53% H_2 in a balance of N_2) and synthetic air (21% O_2 in N_2 , 99.99 % purity). The temperature was ramped by 1°C/min from 50°C to 450°C and back to 50°C with a holding step of 1 hour every 25°C. The conversion of CO was determined on the basis of the amount of CO consumed to form CO_2 and CH_4 . The CO-PrOx experimental conditions used in the magnetometer were simulated in the XRD cell to monitor the bulk phase changes (Co_3O_4 to CoO to Co^0).

3 Result and discussion

3.1 Characterization of model catalyst

The XRD diffraction patterns of the Co_3O_4 samples were collected prior to deposition on the SiO_2 support (see Figure 1). It could be confirmed that all the samples are in the spinel form of cobalt oxide (Co_3O_4) via comparison to the reference pattern 01-073-1701 (face-centred cubic Co_3O_4) from the ICDD PDF2 database. The crystallite sizes of the prepared Co_3O_4 nanoparticles were calculated using Rietveld refinement as well as the Scherrer equation applied to the (100) reflex and are given in Table 1. When compared to the average crystallite sizes obtained from TEM analysis (see figure 2 and table 1), nanoparticles and nanocubes show similar average crystallite sizes, with the nanocubes appearing slightly larger in TEM indicating the possible presence of multiple crystalline domains within one macroscopic cubical structure not distinguishable in TEM. It has to be noted that in the present study large crystallites of the different morphologies, i.e. cubes, sheets, and belt, were targeted to minimize the effects of edge and corner atoms on the observed activity. For the nanosheets and nanobelts, the XRD determined sizes are significantly lower than the morphologies observed in TEM. Closer inspection reveals the presence of small crystallites composing the larger shapes in a form of superstructure. The sizes of these constituting crystallites compare well with the average sizes obtained via XRD.

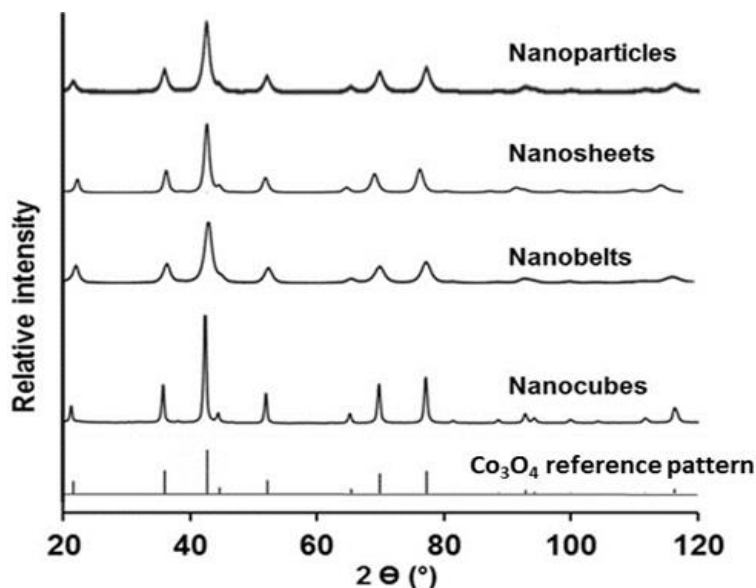


Figure 1: XRD diffractograms of unsupported Co_3O_4 particles and reference pattern for Co_3O_4 .

Table 1: Average crystallite size (nm) of the six samples as obtained from TEM and XRD using Rietveld refinement and the Scherrer equation of the (100) reflex both for the unsupported Co_3O_4 crystallites and supported model catalysts..

Sample	Rietveld refinement ^a (nm)	Scherrer equation ^a (nm)	Rietveld refinement ^b (nm)	TEM based size ^a (nm)	TEM based size ^b (nm)
Nanocubes	34.2 ± 2.9	22.6	33.1 ± 3.2	52 ± 3.4	51 ± 5.6
Nanosheets	13.2 ± 3.2	10.0	12.9 ± 4.7	$13.6 \pm 3.4^*$	
Nanobelts	6.6 ± 1.5	5.0	7.5 ± 3.8	$5.1 \pm 1.2^*$	
Nanoparticles	12.2 ± 2.6	10.5	11.9 ± 3.1	10.9 ± 1.9	10.1 ± 3.2

* TEM sizes of sheets and belts refer to the constituting nano-crystallites not the resulting superstructures.

^a Measurement of the unsupported crystallites.

^b Measurement of the SiO_2 supported crystallites.

The success of the deposition of the prepared Co_3O_4 particles/shapes onto the SiO_2 Stöber spheres was also studied via TEM (see figure 3). While some degree of agglomeration was observed, it could be confirmed that all particles were dispersed on the SiO_2 surface. In the case of the nanosheets, different degrees of interaction of the Co_3O_4 and the carrier were observed, ranging from flat large surface contact to minimal

contact only via an edge. Crystallite size and phase analysis after deposition (XRD and TEM, see table 1 and figure 3) confirms that the cobalt oxide crystallites do not undergo any significant change in size, morphology and or phase upon loading onto the SiO₂ spheres.

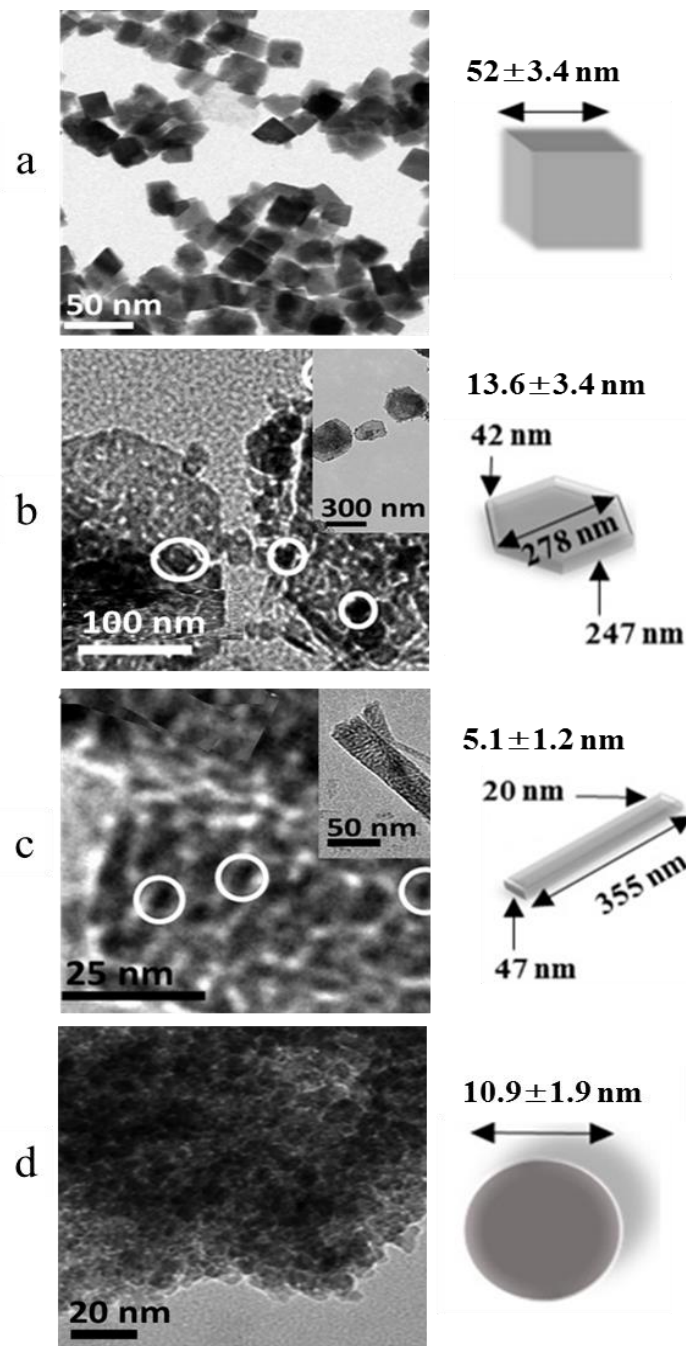


Figure 2: TEM micrographs and average crystallite size for unsupported Co_3O_4 particles for the nanocubes (a), nanosheets (b), nanobelts (c) and Nanoparticles (d).

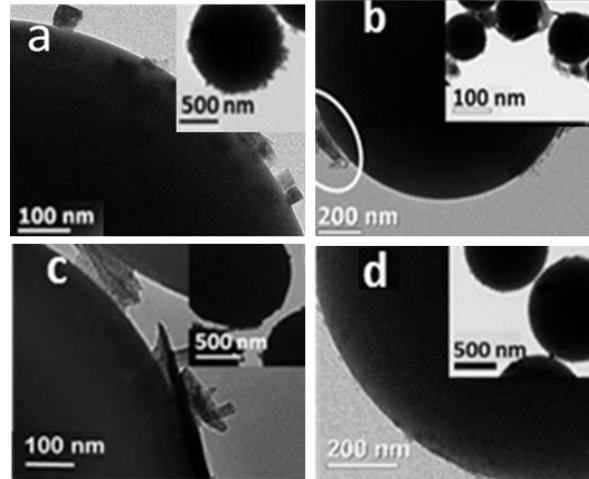


Figure 3: TEM micrographs of supported Co_3O_4 particles for the nanocubes (a), nanosheets (b), nanobelts (c) and Nanoparticles (d).

The concentration of Co_3O_4 on the silica carrier was measured by AAS and ICP (see Table 2) as the loading was not accessible through XRD data due to the non-crystalline nature of the support. The techniques yield very comparable results and close to the targeted 5 wt.-% Co_3O_4 , which supports the effectiveness of the loading method as described in section 2.2.

Table 2: Co_3O_4 loading on SiO_2 in weight percentage as obtained by AAS and ICP.

wt.-% Co_3O_4	Cubes/ SiO_2	Sheets/ SiO_2	Belts/ SiO_2	Nanoparticles/ SiO_2
AAS	4.24	4.60	4.33	4.55
ICP	4.19	4.29	4.29	4.55

The reduction behaviour of the supported oxidic catalysts was studied with temperature programmed reduction (TPR). The multistep reduction was induced by heating the sample in a stream of diluted hydrogen from 60°C to 900°C. The TPR spectra show the major reduction events between 150°C and 500°C which is in agreement with the reduction process of Co_3O_4 , indicating the presence of weak interactions between the Co^{x+} and the surface of the silica support [32, 33]. In principle, the ratio of consumed hydrogen from a first ($\text{Co}^{3+} - \text{Co}^{2+}$) to a second step ($\text{Co}^{2+} - \text{Co}^0$) is 1:3. In the present study, reduction events beyond the theoretically predicted two steps are observed. At most, a total of four peaks can be observed, which are described as the reduction of oxidic cobalt phases (Co_3O_4 , CoO) directly to metallic Co^0 , Co_3O_4 to CoO and cobalt support species (in this case cobalt silica) [35].

For analysis and comparison purposes, the hydrogen consumption of the TPR profiles was normalized and plotted as cumulative consumption as function of temperature (see figure S9). From the gradient of the resulting curves as well as potential points of inflexion, the onsets of distinct reduction events can be compared. Nanoparticles reduce earliest with an onset at approximately 150°C. A second stage reduction evidenced by an increase in hydrogen consumption rate is detected at 225°C. The increased rate could be a result of a catalytic effect of present metallic Co^0 species in the dissociation of gaseous hydrogen. These two stages can be assigned to an initial reduction of some Co_3O_4 to CoO followed by a mix of reduction events from Co_3O_4 to CoO or Co^0 and CoO to Co . Just before reaching the maximum degree of reduction of 96.8%, a third step can be observed at approximately 425°C. This could be a result of cobalt oxide interacting with the support surface. Strong metal support interactions in form of cobalt silicates would be expected to reduce at even higher temperatures.

An initial hydrogen consumption of the nanobelts is registered at comparable temperatures to the nanoparticles. A second reduction event can be measured at 240°C with no significantly increased rate of reduction, reaching maximum DOR_{TPR} at 500°C. Of all samples, the ratio of first to second reduction event is the highest with a ratio of 1:4. The nanosheets reduce initially at 220-240°C with a second reduction event at 300°C and maximum DOR_{TPR} reached at 425-450°C. The reduction temperature of the first

reduction step is significantly higher than in the case of the nanobelts even though XRD and TEM data suggest smaller single crystallites constituting the belts vs the sheets. This observation is in contradiction to previously reported suppressed reduction behaviour for smaller crystallites [22]. Seemingly the environment generated by the superstructure has an additional influence on the reducibility.

The nanocubes reduce to a small extent (low hydrogen consumption) at a temperature as low as 175°C and a second reduction event is recorded at 290°C reaching maximum DOR_{TPR} around 450°C.

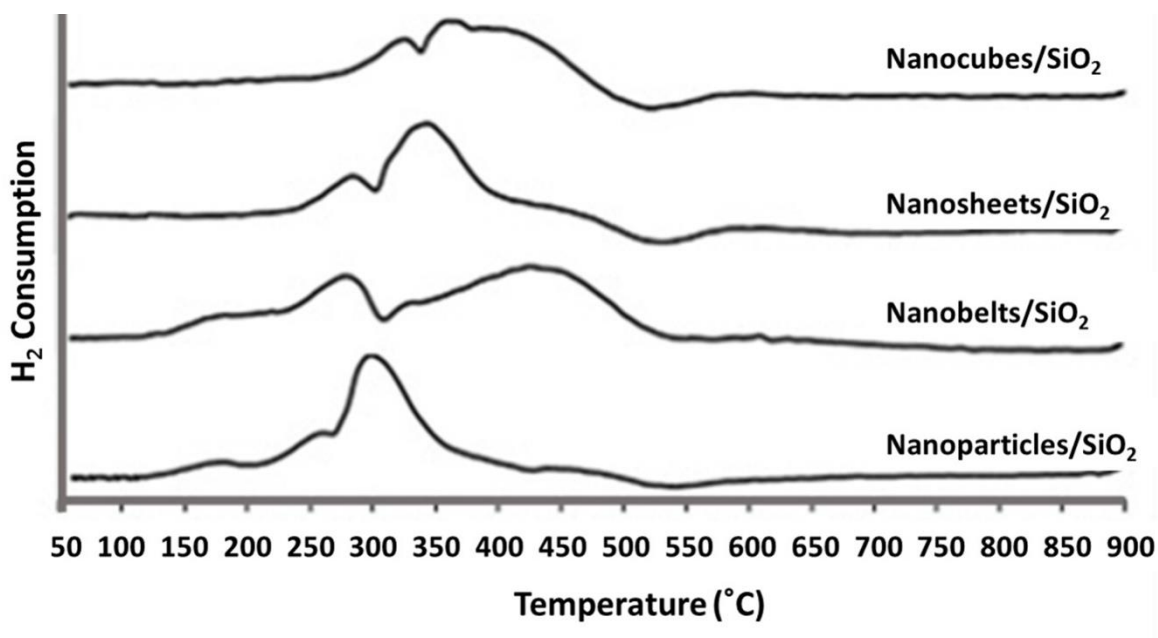


Figure 4: Mass normalised TPR profiles of silica supported Co_3O_4 nanoparticles (Temperature: 900 °C, Heating rate: 5 °C/min, Flow rate: 50 ml(NTP)/min of 5% H_2 in Ar).

In order to further the XRD results, the oxidation states and the composition of fresh $\text{Co}_3\text{O}_4/\text{SiO}_2$ samples of nanocubes, nanosheets and nanobelts were studied with photoelectron spectroscopy. Analysis of Co 2p photoelectron spectra can be difficult due to the closeness in binding energy of Co^{2+} and Co^{3+} states increasing the uncertainty in species quantitation [36], however the satellite structure can be very diagnostic

in the discrimination of these two Co states [36]. With this, the peak shape of the Co 2p spectrum and associated weak satellite structure shown in figure 5 and figure S6–S8, confirms the presence of Co_3O_4 .

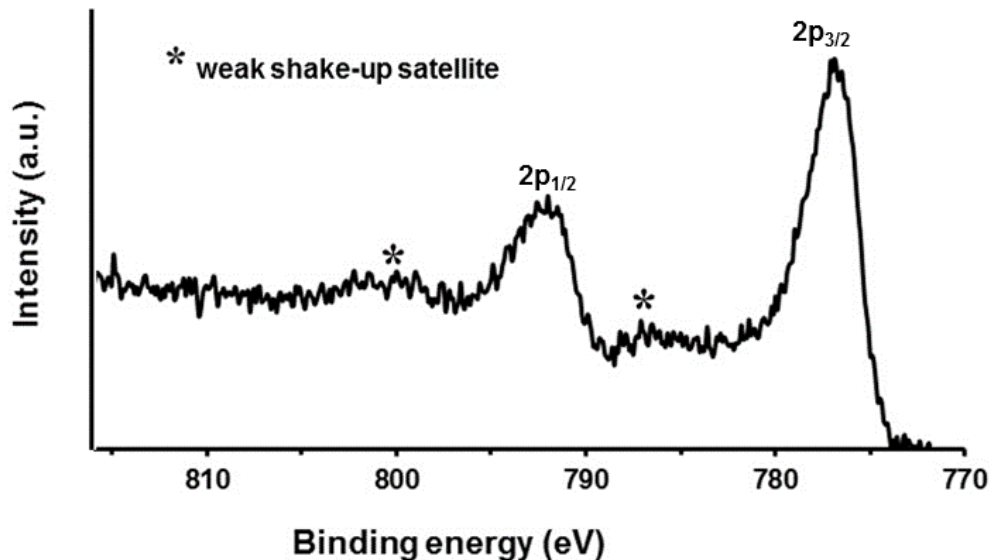


Figure 5: Co 2p XPS profile of the $\text{Co}_3\text{O}_4/\text{SiO}_2$ (nanocubes).

Due to its single crystal morphology, the nanocube sample was further studied *in situ* in the XPS system in a gas treatment cell by heating the sample under a hydrogen atmosphere to the temperatures of the first and second reduction event as observed in TPR (see figure 4). The changes in the Co(2p) spectra are shown in figure 6; clearly the change in the spectral envelope indicates multiple Co oxidation states, and these can be fitted to lineshapes for Co_3O_4 (orange trace) and CoO (blue trace).. These observations are in agreement with the interpretation of the TPR results (figure 4) as the first reduction event (Co^{3+} to Co^{2+}) is expected to yield a mixture of CoO and Co_3O_4 . Further heating to 400°C shows an increase in the CoO state, together with the formation of a peak at 773 eV, consistent with the formation of metallic Co.

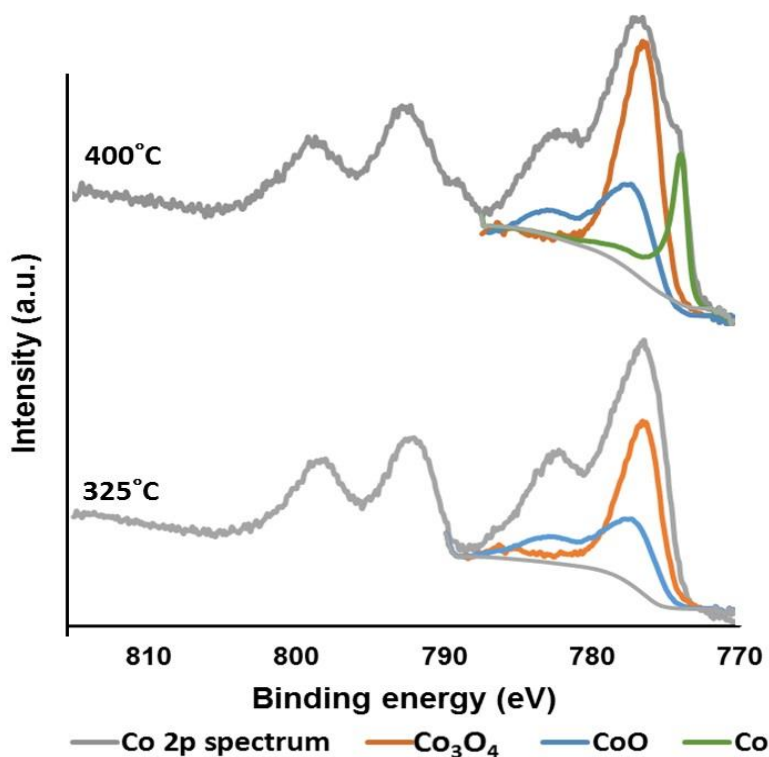


Figure 6: XPS spectra (Co 2p) of $\text{Co}_3\text{O}_4/\text{SiO}_2$ (nanocubes) pre-treated in H_2 at 325°C and 400°C.

In situ CO-PrOx studies were conducted using the in house developed magnetometer and XRD cell. The magnetometer provides information about the formation of even trace amounts of metallic Co^0 , and was used to collect activity and selectivity data. XRD gives direct evidence of the composition of bulk crystalline phases within the instrument specific detection limit. Because of the amorphous nature of the support, which cannot be quantified with XRD, the phase changes were reported as a fraction of the Co-containing species. The low loading combined with a relatively high background stemming from the support resulted in a low signal to noise ratio and calculated concentrations must be regarded as a trend rather than absolute concentration (see figure 7 and 8 B).

To allow comparison with the study previously conducted in our laboratories [22] on the crystallite size dependency of alumina supported Co_3O_4 , Co_3O_4 nanoparticles with an average crystallite size diameter of 10.9 nm were supported on Stöber spheres and incorporated in the present study. Initially, at 50°C, XRD diffraction patterns display, as expected from offline analysis (see figure 1), a pure Co_3O_4 phase on the

amorphous SiO₂ support (see figure 7 A, SiO₂ amorphous contribution omitted for clarity). Analysis of XRD diffraction patterns confirm a stable phase, i.e. the absence of reduction processes, up to temperatures around 200°C, although the peak intensity fades with increasing temperature. It is worth noting that XRD instrument resolution regarding crystallite size or potential shell thickness is limited. Figure 7 D confirms the absence of metallic Co⁰ by the lack of magnetic signal below 200°C. In this temperature range, where the catalyst bulk phase is pure Co₃O₄, CO conversion to CO₂ steadily increases with increasing temperature reaching a maximum conversion of 90.7% at 175°C (see figure 7 C). At these temperatures, with maximum CO oxidation, the conversion of O₂ is 93.3% (feed gas volumetric ratios of CO:H₂ is 1:53 balance N₂), indicating that excess oxygen is nearly quantitatively converted to water at the expense of hydrogen. This is also reflected in a CO₂ selectivity, i.e. the tendency of O₂ to form CO₂ over H₂O, of just under 50%. The hydrogen conversion is measured to be 2.3% which is slightly higher than the expected 1.8% based on the O₂ balance. It can be assumed that the measurement of low conversions will have the highest experimental error associated to it due to fluctuations in the flow rates and integration events of the GC trace.

Beyond 200°C, the Co₃O₄ concentration rapidly decreases in favour of CoO. This event is accompanied by CO-PrOx activity loss, i.e. the decrease of CO conversion and CO₂ concentration in the reactor outlet flow. Moreover, the excess O₂ is fully converted via hydrogen oxidation. At 250°C, the DOR_{mag} measured in the magnetometer increases to 22% signalling the formation of metallic Co⁰. This is paralleled by CH₄ formation. At 450°C (DOR_{mag} is 79%) and throughout the cooling stages, Co⁰ is the only detectable phase. It is worth noting that magnetic readings were taken throughout the experiment including the temperature ramps while XRD diffraction patterns were only collected during temperature holding stages, which explains in part the observed discrepancy in the detection of metallic Co⁰ by the XRD and magnetometer (see figure 7 A and D). During the cooling process, the DOR_{mag} is reduced to 71% at temperatures of 200–175°C as a result of partial oxidation due to the presence of O₂ in the feed gas, possibly resulting in a thin oxide shell. Re-oxidation was also reported in our previous study [22], however at a higher temperature of

250°C which could be a result of a lower maximum DOR_{mag} due to a lower maximum reaction temperature of 350°C.

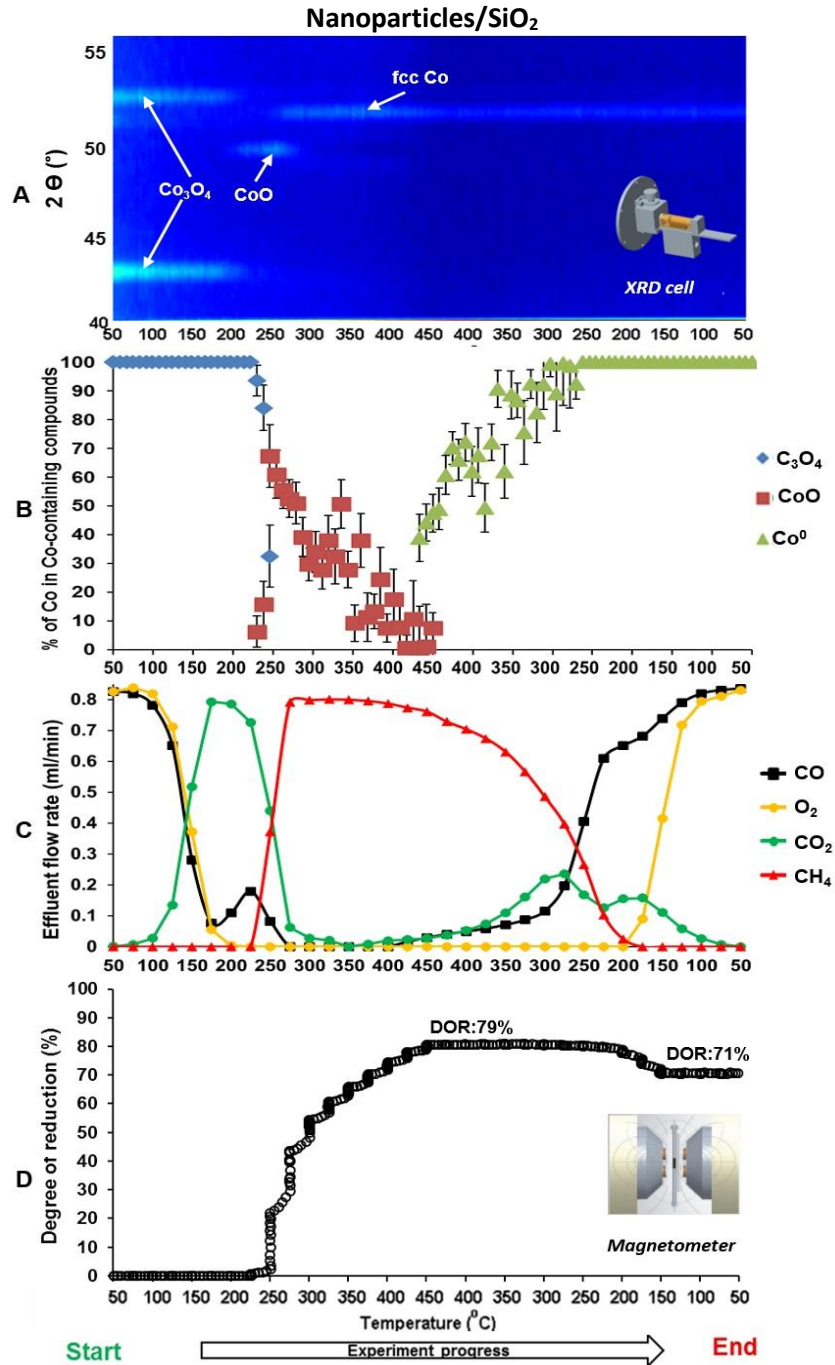


Figure 7: In situ XRD scans and degree of reduction from magnetometer measurements for nanoparticles/SiO₂. A: in situ XRD on top view. B: % of Co in Co-containing compounds. C: effluent flow rate of CO, CO₂, CH₄ and O₂. D:

degree of reduction measured in the magnetometer (50 °C to 450 °C and back to 50 °C holding for 1 hr every 25 °C with a ramp rate of 1 °C/min, magnetic readings: taken at -20, 0, 20 and 0 kOe every 10 min).

In parallel to the reduction to metallic Co^0 , the catalyst selectivity changes drastically. CO_2 formation is reduced to nil at 350°C, while CO is fully consumed by the methanation reaction and O_2 by hydrogen oxidation. In fact, at temperatures above 200°C, O_2 conversion is 100% independent of CO conversion and CO_2 formation, indicating a strong competitive cobalt phase independent hydrogen oxidation reaction (see figure 7 C). Even at full conversion and 100% selectivity of CO to CO_2 (in the absence of methanation), the O_2 conversion should not surpass 50% in the absence of H_2 oxidation. Interestingly the methane formation decreases slightly in the temperature range of 400 to 450°. This can possibly be the result of loss in surface area due to sintering of the cobalt crystallites, reducing the available surface area. Crystallite growth could be confirmed from TEM analysis of the spent sample with an average crystallite size of 13.2 ± 3.4 nm versus 10.9 ± 1.9 nm of the fresh sample (see figure S2). The size increase corresponds to a surface area loss of 17.3%. Nyathi et al. [22] did not observe any significant crystallite growth yet the catalytic and phase behaviour of the nanoparticles supported on SiO_2 is very comparable to the same particles supported on $\gamma\text{-Al}_2\text{O}_3$ up to the maximum temperature in said study, 350°C. Upon lowering the reaction temperature from 450°C, CH_4 formation steadily decreases reaching 0% in the reactor outlet gas stream at 175°C while the CO_2 formation passes through two distinct maxima at 275°C (28.5%) and 175°C (19.1%) without ever achieving the catalytic performance displayed during the initial heating stages. The high temperature maximum is measured without any parallel phase change observed, i.e. it can be assumed that the metallic Co^0 phase has not yet changed during the cooling. However, the lower maximum is accompanied by partial re-oxidation of the catalyst (see figure 7 D). Due similarity in stoichiometry of the Co-PrOx vs the water gas shift reaction (WGS), the origin of CO_2 cannot be determined conclusively by the outlet gas analysis. It can be hypothesized that the WGS reaction is preferred on the metallic surface and through the exothermic nature of the reaction ($\Delta H_{\text{R}} = -41.27$ kJ/mole) increases in rate with decreasing temperature, while on the partially re-oxidized surface the CO-PrOx reaction is supported and explains the low temperature CO_2

formation. The catalytic performance and phase transitions of the Co_3O_4 nanosheets and nanobelts mirror the general trends observed with the nanoparticles (see S1 and S2). Compared to previous studies, we have not been able to synthesize single crystal sheet and belt like structures but rather superstructures constituted of small spherical shaped crystallites.

In direct comparison to the nanoparticles, the tested SiO_2 supported Co_3O_4 cubes show a higher reduction temperature, as already indicated in the TPR measurements (see figure 4). While XRD detected the formation of CoO at temperatures of 200°C in case of the nanoparticles, the nanocubes undergo the first reduction step at temperature of 275°C (see figure 8 A). The reduction to metallic cobalt is similarly delayed and only detected at 300°C (as measured by the magnetometer, see figure 8 D) compared to the $225\text{--}250^\circ\text{C}$ in case of the nanoparticles (see figure 7 D). Although the achieved maximum degrees of reduction are similar, 80% for the nanocubes and 79% for the nanoparticles (all at 450°C), the reduction process differs significantly. The main reduction events of the cubic Co_3O_4 are recorded by the magnetometer at $375\text{--}400^\circ\text{C}$, i.e. $75\text{--}100^\circ\text{C}$ above the initial formation of metallic cobalt. Nanoparticles undergo the dominant reduction directly upon formation of a Co^0 seed at $250\text{--}275^\circ\text{C}$. A similar behaviour is shown by the respective samples in the H_2 -TPR (see figure 4). Interestingly the *in situ* XRD spectra of the nanocubes display clear diffraction lines of CoO throughout the experiment and the Rietveld refinement based pattern analysis yield a concentration of CoO in the cobalt containing phases of 30–40%, which correlates well with the magnetometer based degrees of reduction. It is noted that the diffraction patterns of the nanoparticles show no cobalt bearing phases besides fcc Co^0 beyond temperatures of 425°C . It can be assumed that the relatively small Co_3O_4 crystallites on the nanoparticles (average crystallite size diameter of 10.9 ± 1.89 nm in the fresh catalyst and 13.2 ± 3.36 nm in the spent catalyst) either result in small CoO cores and a metallic shell, with the core diameter below the detection limit of the experimental set-up, or the expected 20–30% oxidic Co (translating to an absolute amount of 1.35 wt.-% based on AAS and ICP loading measurements) is at the given crystallite size below the detection limit. As previously observed by Nyathi [22] and in the present study for the nanoparticles, upon cooling the degree of reduction was reduced.

A re-oxidation of the samples took place at 200–175°C lowering the degree of reduction from 80 to 72% for the nanocubes which represents a relative loss of 13-15%. The quantitative analysis of the XRD diffraction patterns, although it displays a large variance due to the low diffraction line intensity and prominent background of the amorphous SiO₂ carrier, seems to confirm the re-oxidation and suggests the formation of CoO, not Co₃O₄. Similar re-oxidation events are reported in literature for passivation processes [38]. It has to be noted that the re-oxidation of the metallic Co⁰ component coincides with the detection of O₂ in the reactor outlet gas, i.e. the decrease of the O₂ conversion from 100% (see figure 8 C).

Similar to the delayed reduction process, the CO oxidation over the nanocubes requires higher temperatures compared to the nanoparticles. While in the latter case CO₂ is formed at temperature as low as 100°C, temperatures of 175°C are required in the case of nanocubes (see figure 8 C). Due to the later reduction to CoO, the CO oxidation peaks at 250°C with a CO conversion of 67.3% while the maximum CO conversion based purely on oxidation, i.e. in the absence of methane formation, is achieved at 225°C with 58.4%. With a further increase in temperature paralleled by reduction to CoO, both the concentration of CO₂ in the reactor effluent as well as the CO conversion decrease. At the same time the O₂ concentration, which decreased in parallel to the initial CO₂ formation, reaches conversion levels of 100% with a CO₂ selectivity of 42%, again indicating the strong competitive reaction of hydrogen oxidation. As discussed previously, at 100% CO₂ selectivity the O₂ conversion should not surpass 50% as O₂ is available in a twofold excess in the reaction gas mixture. Indeed, the O₂ conversion remains at 100% until reaching the previously mentioned 175°C during the cooling stages. The catalyst shows methanation activity from 325°C onwards, reaching a maximum at 450°C. Although at this stage all converted CO (CO conversion of 95.5%) yields methane, the O₂ conversion is not affected, an indication that hydrogen oxidation can be catalysed on the Co₃O₄, CoO as well as the metallic Co⁰ surface at sufficiently high temperatures [38].

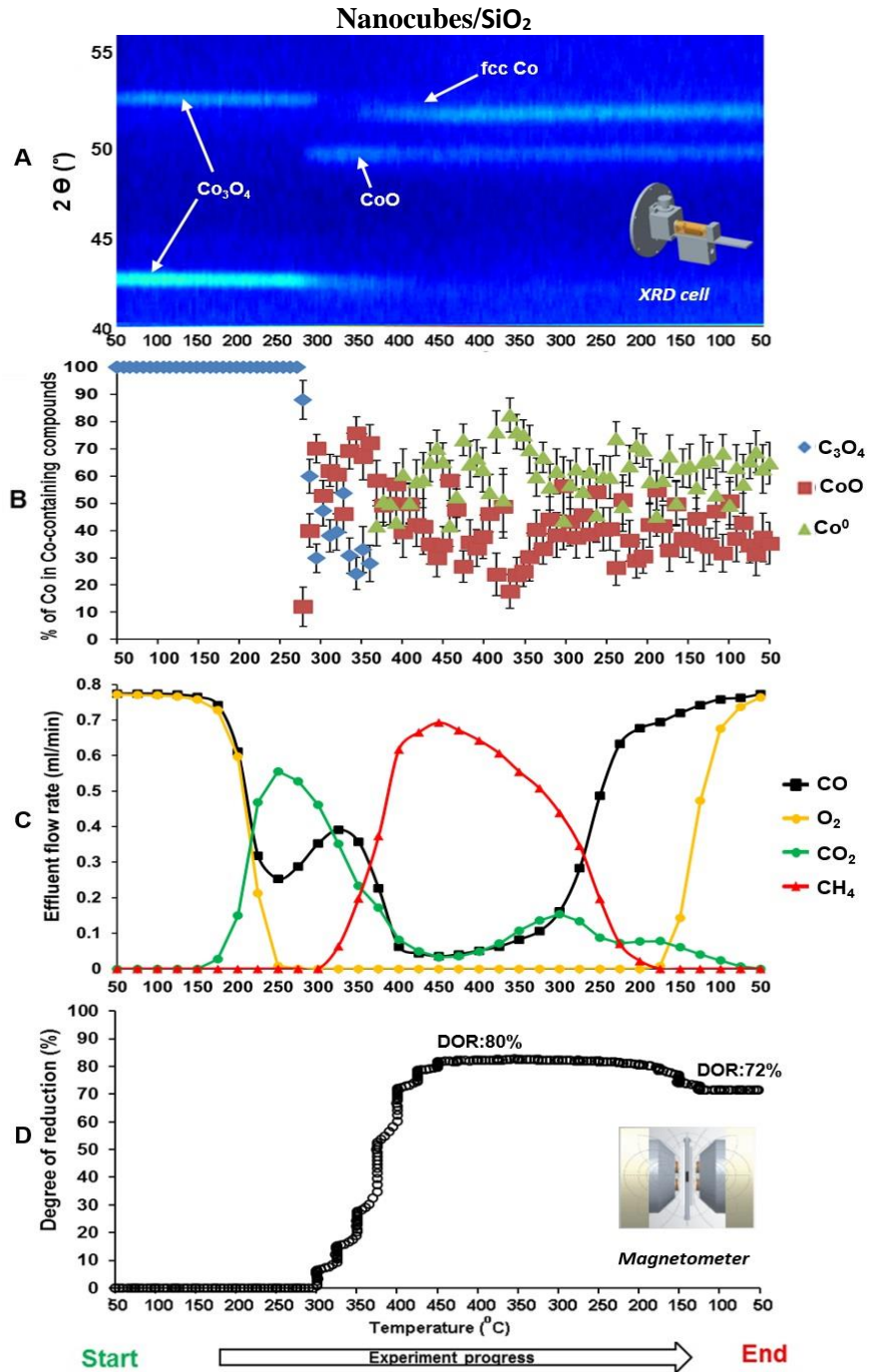


Figure 8: In situ XRD scans and degree of reduction from magnetometer measurements for nanocubes/SiO₂. A: in situ XRD on top view. B: % of Co in Co-containing compounds. C: effluent flow rate of CO, CO₂, CH₄ and O₂. D: degree of reduction measured in the magnetometer (50 $^{\circ}\text{C}$ to 450 $^{\circ}\text{C}$ and back to 50 $^{\circ}\text{C}$ holding for 1 hr every 25 $^{\circ}\text{C}$ with a ramp rate of 1 $^{\circ}\text{C}/\text{min}$, magnetic readings: taken at -20, 0, 20 and 0 kOe every 10 min).

A subsequent lowering of the reaction temperature results in a decrease in CO conversion, a decrease in CH₄ concentration and an increase in CO₂ concentration in the reactor outlet gas. Similar to the previously described nanoparticles, two distinct maxima in CO₂ formation (at 300 and 175°C) are observed. Again, the high temperature maximum cannot be correlated to any phase change, while the low temperature maximum correlates well with the observed re-oxidation. As proposed for the nanoparticles, this could indicate a change of mechanism in CO₂ formation from the potentially Co⁰ catalysed water-gas shift reaction to the oxide, assuming Co³⁺ surface species become available upon re-oxidation, catalysed CO oxidation. The TEM micrographs of the spent samples (see figure S3) show the loss of morphology which was confirmed to occur during the reduction from CoO to Co⁰.

The CO conversion of all model catalysts are shown in Figure up to the temperature at which the first reduction of Co₃O₄ to CoO was observed with *in situ* XRD, i.e the only CO converting reaction under these conditions is the oxidation of CO to CO₂ and no deactivation due to reduction and subsequently no methane formation is observed yet. While the nanoparticles have the highest absolute conversion at the lowest reaction temperature (175°C), the nanocubes display the lowest conversion and require the highest reaction temperature to achieve their best performance (250°C). However, comparing surface specific activities, i.e. the turnover frequencies, as a function of reaction temperature, a very different rating in activity emerges due to the large differences in crystallite size (see figure 10). It is worth noting that for the morphologies identified as superstructures via transmission electron microscopy analysis, i.e. the nanosheets and nanobelts, the surface area of the constituting crystallites was selected for the calculation of the TOF rather than the geometry of the superstructure. To clarify the availability of this surface area, the experimental and theoretical surface areas of the unsupported superstructures were compared. The surface area, based on the TEM average crystallite size of the constituting crystallites as well as Co₃O₄ bulk density, was calculated to be 61 m²/g and 168 m²/g for the nanosheets and nanobelts respectively. Experimentally the surface areas - again of the unsupported superstructures - were determined to be S_{BET, nanosheets} = 69 m²/g and S_{BET, nanobelts} = 184 m²/g, confirming that the constituting crystallites are fully accessible for the catalytic reaction as the

process of supporting onto SiO₂ has been shown to not influence the Co₃O₄ phase. The nanoparticles, nanosheets, and belts catalytically behave similarly, with the observed difference possibly due to the size effect as shown by the work of Nyathi et al. [22]. The nanobelts exhibiting significantly smaller crystallites (5.1 ± 1.2 nm) show a lower turnover frequency when compared to the nanoparticles and nanosheets (10.9 ± 1.89 and 13.6 ± 3.4 nm respectively).

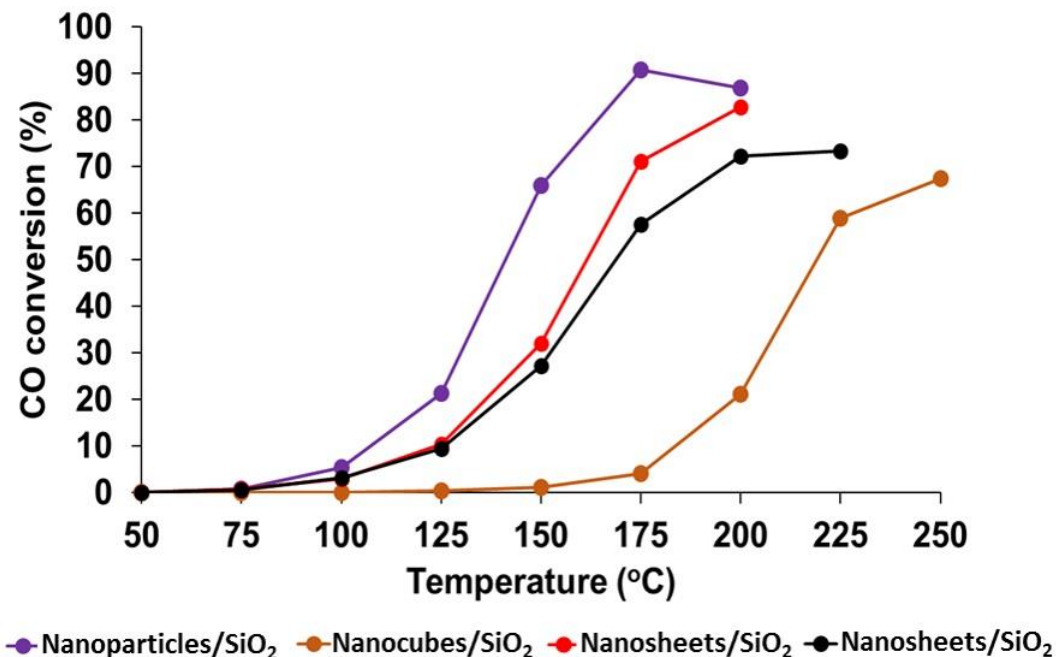


Figure 9: CO conversion of Co₃O₄ model catalysts as a function of temperature.

The previously reported high CO oxidation activity, in the absence of hydrogen in the feed gas stream, of nanosheets and nanobelts due to their high index crystal planes of {112} and {011} respectively [23,41,42] could not be confirmed in the present study as the constituting near spherical nanoparticles are not expected to display any preferred crystal planes.

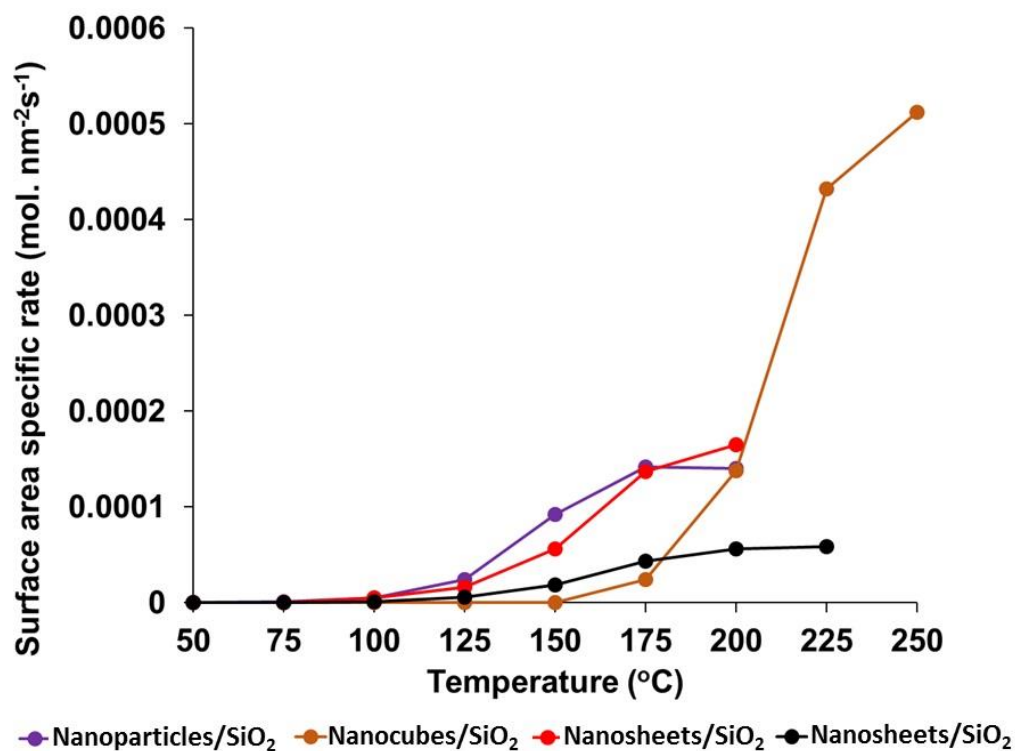


Figure 10: Surface area specific rate of Co_3O_4 model catalysts as a function of temperature.

The prepared nanocubes on the other hand consist of single crystals or at least large crystalline domains which can be expected to exhibit preferentially the {001} planes. With the effect of edge and corner sites minimized due to the relatively large size, the observed turnover frequency of the nanocubes surpasses that of other catalysts by a factor of 3.5 to 4 (see Figure). Their low conversion and the required high reaction temperature could potentially be overcome by increasing the active surface area of the crystallites, i.e. using smaller cubes as have been synthesized in our research group [33, 37].

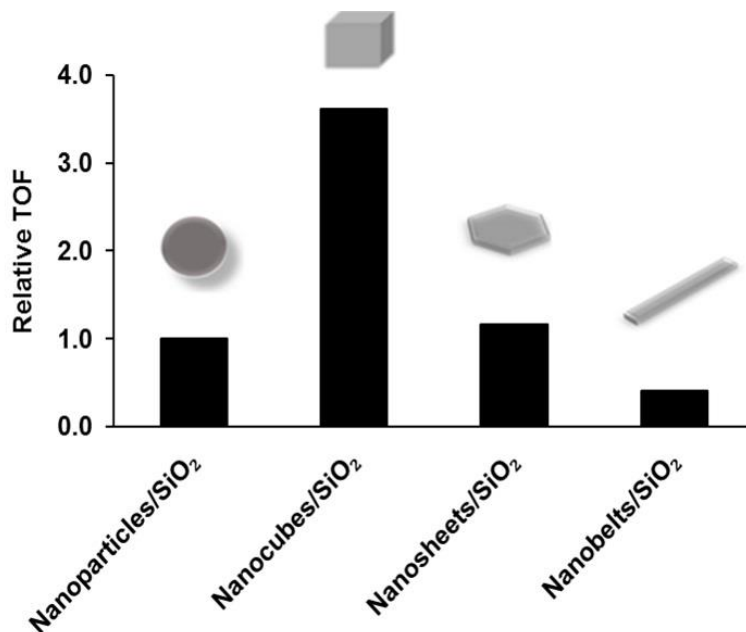


Figure 11: Relative turnover frequency as normalised to nanoparticles/SiO₂ (Temperatures at highest TOF; nanoparticles/SiO₂: 175 °C, nanocubes/SiO₂: 250 °C, nanosheets/SiO₂: 200 °C, nanobelts/SiO₂: 225 °C).

4 Conclusion

It was attempted to synthesize Co₃O₄ particles of three different morphologies (nanocubes, sheets and belts). Closer characterization of the prepared materials revealed that the nanosheets and nanobelts are in fact superstructures comprising of small crystallites instead of single crystals. These crystallites - BET analysis confirms their full accessibility for the reaction - behave catalytically similar to the near-spherical nanoparticles previously reported [22] and studies here as baseline. The lower surface specific activity of the crystallites comprised in the nanobelt superstructures can be rationalized by the reported crystallite size effect of Co₃O₄ in the preferential oxidation of CO [22]. The nanocubes on the other hand, are single crystallites or at least large crystalline domains preferentially exposing the {001} facets. These crystallites require a significantly higher reaction temperature to show activity for CO oxidation, i.e. surface and bulk Co³⁺ atoms are stabilized against reduction to Co²⁺ compared to the near spherical nanoparticles, and due to their low mass specific surface area are inferior with regards to absolute conversion. However, a

comparison of the surface specific activity at maximum conversion clearly shows that the preferential {001} facets of the nanocubes outperform the other studied model catalysts by a factor of 3.5. This observation underlines the importance of catalyst morphology and provides an additional handle for the design of catalysts. In the cubic system, the overall lower CO conversion can potentially be overcome by reducing the size of the crystallites. The resulting increase in edge and corner sites as well as the effect on reducibility is currently under investigation. Based on the here presented results and previous studies which have identified the {112} facets to even outperform {001} planes in CO oxidation activity in absence of H₂ [21,24], stable Co₃O₄ single crystallites preferentially exposing said facets should be synthesized and studied in the CO-PrOx reaction.

Acknowledgements

The authors would like to thank c*change (DST-NRF Centre of Excellence in Catalysis), the Newton Fund and the Royal Society in form of the Newton Advanced Fellowship program, the Catalysis Institute at the Department of Chemical Engineering, University of Cape Town and the Cardiff Catalysis Institute and for their financial and experimental support.

The help from Mohamed Jaffer, Innocent Shuro and Miranda Waldron from the Electron Microscope Unit, Zulfa le Riche and Jessica Heynes for AAS/ICP and BET analysis, Rachel Cupido, Waldo Koorts, Gideon Kaufmann and Chantal Le Roux at the University of Cape Town is much appreciated.

References

- [1] J. J. Baschuk, & X. Li, *Int. J. Renew. Energy Res.* 25 (2001) 695–713.
- [2] N.V. Gnanaprasam, B.V. Reddy, M.A. Rosen, *Int. J. Hydrogen Energy* 35 (2010) 4933–4943.

- [3] S. Freni, G. Calogero, S. Cavallaro, J. Power Sources 87 (2000) 28–38.
- [4] W. Deng, J. De Jesus, H. Saltsburg, M. Flytzani-Stephanopoulos, Appl. Catal. A: Gen. 291 (2005) 126–135.
- [5] P.K.T. Liu, Media and process technology inc. (2010) 62–66.
- [6] N.R. Udengaard, Preprints of Papers- ACS, Division of Fuel Chemistry, 49 (2004) 906–907.
- [7] T. Hayashi, K. Tanaka, M. Haruta, J. Catal. 178 (1998) 566–575.
- [8] M. Lomello-Tafin, A.A. Chaou, F. Morfin, V. Capsb, J. Rousset, Chem. Comm. (2005) 388–390.
- [9] D. Gavrila, A. Georgakab, V. Loukopoulosb, G. Karaiskakisb, B.E. Nieuwenhuysa, Gold Bulletin (2006) 192–199.
- [10] E. Quinet, F. Morfin, F. Diehl, P. Avenier, V. Caps, J. Rousset, Appl. Catal. B: Environ. 80 (2008) 195–201.
- [11] G. Avgouropoulosa, T. Ioannidesa, H. Matralis, Appl. Catal. B: Environ. 56 (2005) 87–93.
- [12] E. Morettia, M. Lenardaa, L. Storaroa, A. Talona, R. Frattinib, S. Polizzib, E. Rodríguez-Castellón, A. Jiménez-López, Appl. Catal. B: Environ. 72 (2007) 149–156.
- [13] W. Liu, M. Flytzanistephanopoulos, J. Catal. 153 (1995) 304–316.
- [14] B. Sköarman, D. Grandjean, R.E. Benfield, A. Hinz, A. Andersson, L.R. Wallenberg, J. Catal. 211 (2002) 119–133.
- [15] D. Gamarra, A. Martinez-Arias, J. Catal. 263 (2009) 189–195.
- [16] S. C. Petitto, E. M. Marsh, G.A. Carson, M.A. Langell, J. Mol. Catal. A 281 (2010) 49–58.
- [17] M.P. Woods, P. Gawade, B. Tan, U.S. Ozkan, Appl. Catal. B: Environ.. 97 (2010) 28–35.
- [18] Z. Zhao, M. Yung, U. S. Ozkan, Catal. Comm. 9 (2008) 1465–1471.
- [19] K. Omata, Y. Kobayashi, M. Yamada, Catal. Comm. 6 (2005) 563.
- [20] S. Özkara, A.N. Akin, Z. Misirli, A.E. Aksoylu, Turk. J. Chem. 29 (2005) 219–224.
- [21] L. Hu, K. Sun, Q. Peng, B. Xu, Y. Li, Nano Research 3 (2010) 363–368.

- [22] T. Nyathi, N. Fischer, A. York, M. Claeys, *Faraday Diss.* 197 (2017) 269-285.
- [23] L. Hu, Q. Peng, Y. Li, *J. Am. Chem. Soc.* 130 (2008) 16136–16137.
- [24] S. Cao, F. Tao, Y. Tang, Y. Lia, J. Yu, *Chem. Soc. Rev.* 45 (2016) 4747–4765
- [25] Q. Wang, Y. Xia, C. Jiang, *Cryst. Eng. comm.* 16 (2014) 9721–9726.
- [26] N. Fischer, E. van Steen, M. Claeys, *Catal. Tod.* 171 (2011) 174-179.
- [27] N. Fischer, T. Feltes, M. Claeys, *CRC – Concise Encyclopaedia of Nanotechnology, Chapter 45*, ISBN 9781466580343 (2015) 547–560.
- [28] W. Stöber, A. Fink, *J. Colloid Interf. Sci.* 69 (1968) 62–69.
- [29] M. Claeys, N. Fischer, Patent No. PCT patent WO2013/005180 A1. 5180, (2013).
- [30] N. Fischer, B. Clapham, T. Feltes, E. van Steen, M. Claeys, *Angew. Chem. Int. Ed.* 53 (2014) 1342-1345.
- [31] M. Claeys, E. van Steen, J. Visagie, J. van de Loosdrecht, Patent No. PCT patent WO 2010/004419 A2. 4419, (2010).
- [32] M. Wolf, N. Fischer, M. Claeys, *Catal. Today*, 275 (2016) 135–140.
- [33] A.C.F. Holm, A. Clark, *J. Catal.* 11 (1968) 305-316.
- [34] N. Fischer, M. Minnermann, M. Baeumer, E. van Steen, M. Claeys, *Catal. Lett.* 142 (2012) 830–837.
- [35] G. Jacobs, Y. Ji, B.H. Davis, D. Cronauer, A.J. Kropf, C.L. Marshall, *Appl. Catal. A: Gen.* 333 (2007) 177–191.
- [36] M.C. Biesinger, B.P. Payne, A.P. Grosvenor, L.W.M. Lau, A.R. Gerson, R.St.C. Smart, *Appl. Surf. Sci.* 257 (2011) 2717.
- [37] M. Wolf, H. Kotzé, N. Fischer, M. Claeys, *Faraday Diss.* 197 (2017) 243-268.
- [38] L. Lukashuk, K. Föttinger, E. Kolar, C. Rameshan, D. Teschner, M. Hävecker, *J. Catal.* 344 (2016) 1–15.
- [39] M. Claeys, M. E. Dry, E. van Steen, E. du Plessis, P. J. van Berge, A. M. Saib and D. J. Moodley, *J. Catal.* 318 (2014) 193–202.
- [40] M.C. Biesinger, B.P. Payne, A.P. Grosvenor, L.W.M. Lau, A.R. Gerson, R.St.C. Smart, *Appl. Surf. Sci.* 257 (2011) 2717–

2730.

[41] X. Xie, Y. Li, Z.Q. Liu, M. Haruta, W. Shen, *Nature* 458 (2009) 746.

[42] Y. Yu, T. Takei, H. Ohashi, H. He, X. Zhang, M. Haruta, *J. Catal.* 267 (2009) 121–128.